BIOLOGY OF REPRODUCTION **85,** 690–701 (2011)
Published online before print 29 June 2011.
DOI 10.1095/biolreprod.111.091132

Loss of SPEF2 Function in Mice Results in Spermatogenesis Defects and Primary Ciliary Dyskinesia[1]

Anu Sironen,[3] Noora Kotaja,[4] Howard Mulhern,[5] Todd A. Wyatt,[6] Joseph H. Sisson,[6] Jacqueline A. Pavlik,[6] Mari Miiluniemi,[3] Mark D. Fleming,[5] and Lance Lee[2,7,8]

Biotechnology and Food Research,[3] Animal Genomics, MTT Agrifood Research Finland, Jokioinen, Finland
Department of Physiology,[4] Institute of Biomedicine, University of Turku, Turku, Finland
Department of Pathology,[5] Children's Hospital Boston, Boston, Massachusetts
Pulmonary and Critical Care Medicine Section,[6] Department of Internal Medicine, University of Nebraska Medical Center, Omaha, Nebraska
Sanford Children's Health Research Center,[7] Sanford Research/University of South Dakota, Sioux Falls, South Dakota
Department of Pediatrics,[8] Sanford School of Medicine, University of South Dakota, Sioux Falls, South Dakota

ABSTRACT

Primary ciliary dyskinesia (PCD) results from defects in motile cilia function. Mice homozygous for the mutation big giant head (*bgh*) have several abnormalities commonly associated with PCD, including hydrocephalus, male infertility, and sinusitis. In the present study, we use a variety of histopathological and cell biological techniques to characterize the *bgh* phenotype, and we identify the *bgh* mutation using a positional cloning approach. Histopathological, immunofluorescence, and electron microscopic analyses demonstrate that the male infertility results from shortened flagella and disorganized axonemal and accessory structures in elongating spermatids and mature sperm. In addition, there is a reduced number of elongating spermatids during spermatogenesis and mature sperm in the epididymis. Histological analyses show that the hydrocephalus is characterized by severe dilatation of the lateral ventricles and that *bgh* sinuses have an accumulation of mucus infiltrated by neutrophils. In contrast to the sperm phenotype, electron microscopy demonstrates that mutant respiratory epithelial cilia are ultrastructurally normal, but video microscopic analysis shows that their beat frequency is lower than that of wild-type cilia. Through a positional cloning approach, we identified two sequence variants in the gene encoding sperm flagellar protein 2 (SPEF2), which has been postulated to play an important role in spermatogenesis and flagellar assembly. A causative nonsense mutation was validated by Western blot analysis, strongly suggesting that the *bgh* phenotype results from the loss of SPEF2 function. Taken together, the data in this study demonstrate that SPEF2 is required for cilia function and identify a new genetic cause of PCD in mice.

cilia, flagella, genetics, hydrocephalus, male infertility, primary ciliary dyskinesia, sinusitis, SPEF2, spermatogenesis

INTRODUCTION

Spermatogenesis is a complex developmental process whereby immature diploid spermatogonia differentiate into haploid spermatozoa [1–12]. During the cycle of the seminiferous epithelium, spermatogonia undergo several rounds of mitosis, eventually resulting in the formation of spermatocytes, which subsequently undergo two meiotic divisions to form round spermatids [1–4, 8–12]. The process concludes with spermiogenesis, during which spermatids elongate to form spermatozoa [1–4, 8–12]. This phase of spermatogenesis involves reorganization of the organelles, condensation of nuclear chromatin, formation of the acrosome, elimination of the cytoplasm, and formation and elongation of the flagellum [3, 4, 11, 13]. Throughout germ cell differentiation, somatic Sertoli cells nurture the developing sperm cells, regulate proper germ cell movement, and maintain the integrity of the seminiferous tubules [14, 15]. The sperm cells are released into the lumen of the seminiferous tubule of the testis by a process known as spermiation and subsequently migrate to the epididymis [7, 10–12].

The sperm flagellum extends from the spermatid centrosome during spermiogenesis and is comprised of four segments extending distally from the cytoplasm: the connecting piece, the middle piece, the principal piece, and the end piece [7, 16]. The axoneme, or the flagellar core, generates the motor force required for flagellar bending [7, 17]. After axoneme formation, several accessory structures are assembled as spermiogenesis progresses. Outer dense fibers line the middle piece and the principal piece and play roles in protecting the structural integrity of the flagellum and regulating the flagellar waveform [7, 18]. The outer dense fibers are assembled around the axoneme in a proximal to distal direction that extends toward the end piece and are covered by mitochondria along the middle piece [7, 18–21]. The fibrous sheath lines the principal piece, where it provides flagellar tension and flexibility and serves as a site for signal transduction molecules and glycolytic enzymes [7, 22]. In contrast to the outer dense fibers, the fibrous sheath is assembled in a distal to proximal direction as the principal piece is formed [19, 21, 23] and is attached to the outer dense fibers at the proximal end of the principal piece, replacing two of the outer dense fibers in the principal piece [22].

The axoneme of sperm flagella as well as motile cilia on respiratory and oviduct epithelial cells, ependymal cells on the ventricular surface of the brain, and nodal cells in the early embryo, is comprised of a so-called 9+2 microtubule

[1]Supported by the March of Dimes (6-FY07-397 to M.D.F.), Academy of Finland (A.S., N.K., and M.M.), and the National Institutes of Health (R01AA017993-3 to T.A.W.; 5R37AA008769-19 to J.H.S.). Sequence of mouse *Spef2* deposited with GenBank and released under accession number HQ856050.
[2]Correspondence: FAX: 605 312 6071;
e-mail: Lance.Lee@sanfordhealth.org

Received: 17 January 2011.
First decision: 15 February 2011.
Accepted: 16 June 2011.

eISSN: 1529-7268 http://www.biolreprod.org
ISSN: 0006-3363

arrangement, with nine outer microtubule doublets surrounding a single central pair [17, 24–28]. Inner and outer dynein arms associated with the outer microtubule doublets provide the motor force required for ciliary and flagellar beating [17, 26]. In addition, nexin links consist of the dynein regulatory complex and connect the neighboring outer microtubule doublets, while radial spokes link the outer doublets to the central pair [17, 26]. Unlike respiratory epithelial cilia, ependymal cilia, and sperm flagella, nodal cilia have a 9+0 structure that lacks the central microtubule pair [17, 26]. The ciliary and flagellar axoneme is formed through a process known as intraflagellar transport (IFT) where axonemal proteins synthesized in the cytoplasm are transported through the elongating cilia and flagella by IFT proteins [29]. Transport is dependent on motor proteins kinesin 2, which drives anterograde transport toward the distal tip, and cytoplasmic dynein 1b, which drives retrograde transport back toward the cytoplasm [29].

While sperm flagella are required for cell motility, respiratory epithelial cilia are responsible for clearance of mucus, ependymal cilia are required for proper flow of cerebrospinal fluid (CSF), and nodal cilia are required for proper left-right patterning in the early embryo [24, 25, 27]. Defects in motile ciliary and flagellar function commonly result in the syndrome termed primary ciliary dyskinesia (PCD), which was previously referred to as immotile cilia syndrome. PCD affects approximately 1 in 16 000 people worldwide, and patients commonly suffer from chronic sinusitis, bronchiectasis, neonatal respiratory distress, male infertility, and situs inversus, a randomization of left-right asymmetry [17, 30–32]. The specific presentation of bronchiectasis, sinusitis, and situs inversus is a subset of PCD that is also referred to as Kartagener's syndrome. Occasionally, hydrocephalus [33–38], otitis media [39–46], female infertility [39, 47–50], and retinitis pigmentosa [51–53] are also associated with PCD.

Several genes have been implicated in PCD in human patients and mouse models [17, 54]. Many of these genes encode ciliary components, including dynein heavy chains DNAH5 [55–58], DNAH7 [59], and DNAH11 [60–62], dynein intermediate chains DNAI1 [41, 63] and DNAI2 [42], central pair complex proteins HYDIN [64–68], sperm-associated antigen 6 (SPAG6) [69–71], sperm-associated antigen 16L (SPAG16L) [71–73], PCD protein 1 (PCDP1) [74, 75], and radial spoke proteins RSPH9 and RSPH4A [76]. Additional ciliary proteins implicated in PCD include the IFT protein Polaris [77, 78], the structural protein tektin-t [79], and the leucine-rich-repeat (LRR)-containing protein LRRC50 [39, 80]. In addition, several nonciliary proteins have also been implicated in PCD, including transcription factors FOXJ1/HFH4 [81, 82] and heat shock transcription factor 1 (HSF1) [83], the retinitis pigmentosa GTPase regulator (RPGR) [51–53], DNA polymerase lambda [84], thioredoxin family member TXNDC3 [40], dynein assembly factor kintoun (KTU, official symbol DNAAF2) [45], canonical WNT pathway inhibitor chibby [85], adenylate kinase 7 (AK7) [86], and tubulin tyrosine ligase-like 1 (TTLL1) [87, 88]. Proteomic analyses from humans [89] and the flagellated unicellular eukaryote *Chlamydomonas reinhardtii* [90] have indicated that the cilium contains approximately 700 different proteins. Given the complexity of this organelle, it is likely that other genes may yet be implicated in mammalian PCD.

Identification of new mouse models of PCD will identify the requirement of ciliary proteins in cilia function and further uncover the mechanisms underlying ciliary motility. In this article, we describe an autosomal recessive mouse mutation that results in severe hydrocephalus and has been named big giant head (*bgh*). Consistent with PCD, affected animals also have sinusitis and male infertility. Using a positional cloning approach, this study demonstrates that a mutation in the gene encoding sperm flagellar protein 2 (SPEF2) results in the PCD phenotype in *bgh* homozygotes. *Spef2*, which is also known as *Kpl2*, is specifically expressed in ciliated cell types [91, 92]. An intronic insertion affecting splicing of a testis-specific isoform of *Spef2* results in the immotile short-tail sperm defect in Finnish Yorkshire pigs [93]. Interaction with the IFT protein IFT20 in the mouse testis suggests that SPEF2 may play a role in flagellar biogenesis [92]. Consistent with this role, we show that the infertility in *bgh* males results from reduction in the number of elongating spermatids during spermiogenesis and structural defects in sperm flagella. In contrast, we also demonstrate that the mutation in *Spef2* causes only a reduction in respiratory ciliary beating without causing ultrastructural defects, indicating that SPEF2 is required for both ciliary motility and spermatogenesis.

MATERIALS AND METHODS

Mice

The *bgh* mutation arose from animals in a line maintaining the fragile red mutation [94], which was generated by N-ethyl-N-nitrosourea (ENU) mutagenesis on the C57BL/6J (B6) background and maintained on a mixed C57BL/6J;C57BL/10J (B6;B10) background. The *bgh* mutation was backcrossed to and maintained on the B6 and 129S6/SvEvTac (129) backgrounds and mapped by crossing to BALB/cByJ (BALB). Analysis of hydrocephalus was performed on B6 animals at 3–4 wk of age. Analysis of spermatogenic defects was performed on (B6x129)F1 (B6129F1) animals at greater than 8 wk of age. Analysis of sinusitis was performed on both B6 animals at 3–4 wk of age and B6129F1 mice at greater than 8 wk of age. All the animal procedures were approved by the Institutional Animal Care and Use Committee at Children's Hospital Boston and the Committee on the Ethics of Animal Experimentation at the University of Turku in accordance with the *Guide for Care and Use of Laboratory Animals* (National Academy of Science).

Histology

Brains were fixed in 10% buffered formalin, and heads, testes, and epididymides were immersion fixed in Bouin fixative. Once the bones in the heads were fully decalcified, coronal sections were cut through the maxillary sinuses. All the tissues were embedded in paraffin, sectioned, and stained with hematoxylin and eosin. Analysis of brain histology was performed on four *bgh* mice and four wild-type controls. Analysis of testis histology was performed on five *bgh* mice and four wild-type controls, and analysis of epididymis histology was performed on two *bgh* mice and one wild-type control. Finally, analysis of maxillary sinus histology was performed on eight *bgh* mice and eight wild-type controls on the B6 background as well as two *bgh* mice and two wild-type controls on the mixed B6129 background.

Spermatozoa Preparations

Spermatozoa collected from the cauda epididymis were diluted in PBS and spread on slides. Epididymal sperm from two *bgh* mice and one wild-type control were analyzed by light microscopy.

Squash Preparations

Testes were dissected, decapsulated, staged, sectioned, and visualized by phase contrast microscopy as previously described [95]. Squash preparations were performed on testes from one *bgh* mouse and one wild-type control.

Drying Down Preparations

Stage-specific segments of seminiferous tubules were isolated, and cells were released and fixed on slides as described previously [95]. Preparations from two *bgh* and one wild-type control were visualized by phase contrast microscopy and used for immunofluorescence.

Immunofluorescence

Sperm slides and drying down preparations were postfixed with 4% paraformaldehyde for 15 min and permeabilized with 0.2% Triton X-100 for 5 min. Nonspecific sites were blocked in 10% normal goat serum and 3% bovine serum albumin in PBS. Samples were probed with an anti-AKAP4 monoclonal antibody (1:200; BD Biosciences) or an anti-acetylated tubulin monoclonal antibody (1:500; Sigma Aldrich). Mouse immunoglobulin G (IgG) (1:500) was used as a negative control. Alexa Fluor 488 or 594 goat anti-mouse IgG (1:500; Molecular Probes) was used as a secondary antibody. For detection of mitochondria, slides were incubated with 200 nM Mitotracker (Invitrogen) in PBS for 15 min. Fluorescence was visualized on a Leica DMRB fluorescence microscope.

Electron Microscopy

Tracheae from six *bgh* mice and one wild-type control were fixed overnight in a modified Karnovsky solution containing 2.5% glutaraldehyde and 2.0% paraformaldehyde, pH 7.4. Fixed tissues were rinsed in cold 0.1 M sodium cacodylate buffer, pH 7.4 and treated with cacodylate-buffered 2.0% osmium tetroxide for 1.5 h. The tissues were dehydrated, embedded, cut, stained, and visualized as previously described [75]. Testis and epididymal sperm samples were fixed in 5% glutaraldehyde and treated with a potassium ferrocyanide-osmium fixative. The samples were embedded in epoxy resin (glycidether 100; Merck), sectioned, stained with 5% uranyl acetate and 5% lead citrate, and visualized on a JEOL 1200 EX electron microscope. Testes were analyzed from three *bgh* mice and two wild-type controls, and epididymal sperm was analyzed from two *bgh* mice and one wild-type control.

Ciliary Beat Frequency Analysis

Tracheae from 3- to 4-wk-old B6 mice were isolated in Dulbecco modified Eagle medium supplemented with 1% penicillin-streptomycin. The ciliary beat frequency was analyzed using the Sisson-Ammons video analysis system as previously described [75, 96]. Tracheae were analyzed from nine *bgh* mice and nine wild-type controls.

Positional Cloning

To map the *bgh* mutation, we crossed B6 heterozygotes to wild-type BALB animals and backcrossed the confirmed heterozygous (B6xBALB)F1 (B6BALBF1) animals to their heterozygous B6 parent to generate affected N2 progeny. Using the Harvard Medical School-Partners Healthcare Genetics and Genomics Core Facility, we mapped the mutation to the proximal region of chromosome 15 by genotyping 11 affected N2 animals with a genomewide panel of single nucleotide polymorphism (SNP) markers. Fine mapping with microsatellite repeat markers in a total of 18 affected N2 animals refined the interval to an approximately 8 Mb region between 3.9 and 12.2 Mb. The proximal end of this interval is defined by a microsatellite marker (F: GCAAGGGTTAGATGGGTGTC; R: CACCCTCAAATCCCTCATTC) at 3.9 Mb that amplifies 24 CA repeats in B6 and 22 CA repeats in BALB. The distal end is defined by SNP marker rs13482436 (F: CCATGGGTTCCCT TATTTCC; R: GCCAGGGGATTTTTGTTAGG) at 12.2 Mb, where the polymorphic base is G in B6 and C in BALB.

Spef2 *Gene Annotation*

The *Spef2* gene structure was determined using the following methods: 1) online gene prediction programs GeneMark (exon.biology.gatech.edu/eukhmm.cgi) [97] and GenScan (genes.mit.edu/GENSCAN.html) [98], 2) alignment with predicted human exons, 3) sequencing of predicted mouse exons from genomic DNA, and 4) sequencing of reverse transcribed *Spef2* cDNA. Predicted protein domains were determined using the NCBI Conserved Domains search (www.ncbi.nlm.nih.gov/Structure/cdd/wrpsb.cgi?) [99]. Sequences were analyzed using the Sequencher software (Gene Codes).

Genomic Sequencing

Genomic DNA was isolated from wild-type and *bgh* mouse tails using the Puregene tissue kit (Qiagen). *Spef2* exons were amplified by PCR and sequenced. Sequences were analyzed using the Sequencher software. All 37 exons were initially sequenced in one *bgh* heterozygote, and each exon containing a putative disease variant, which was identified by two peaks in the chromatogram, was sequenced in more than 100 animals comprised of wild types, heterozygotes, and *bgh* homozygotes. Heterozygotes were confirmed by breeding, and *bgh* homozygotes were confirmed by phenotypic analysis.

Reverse Transcription Polymerase Chain Reaction

RNA was isolated from one wild-type B6 testis using the RNeasy kit (Qiagen), and first-strand cDNA was synthesized from 1 μg of total RNA using the SuperScript III First Strand reverse transcription kit (Invitrogen). Twelve overlapping segments spanning the entire predicted *Spef2* cDNA were amplified and sequenced to determine the complete cDNA sequence. Sequences were analyzed using the Sequencher software.

Western Blot Analysis

Wild-type and *bgh* testes from three *bgh* mice and two wild-type controls were homogenized in 1% Triton X-100 in PBS. Proteins were separated by SDS-PAGE, transferred to polyvinylidene fluoride (PVDF) membrane, and blocked in 1% nonfat dry milk in TBS (10 mM Tris base, 150 mM sodium chloride; pH 8.0) with 1% Tween-20 (TBS-T). Blots were probed with polyclonal anti-SPEF2 antibody (1:250) [92] or monoclonal anti-acetylated tubulin antibody (1:2000, Sigma-Aldrich) and detected with horseradish peroxidase-conjugated anti-rabbit or anti-mouse secondary antibodies, respectively (1:10 000, GE Healthcare). Proteins were visualized by enhanced chemiluminescence (Perkin-Elmer) according to the manufacturer's instructions and exposed to film.

Nucleotide Sequence Accession Number

The cDNA sequence for mouse *Spef2* derived from wild-type C57BL/6J testis was deposited in GenBank as accession number HQ856050.

RESULTS

bgh *Mice Have Hydrocephalus*

A mutation causing hydrocephalus occurred in mice on a mixed C57BL/6J;C57BL/10J background (Fig. 1). The mutation was heritable, and the number of affected animals was consistent with an autosomal recessive mode of inheritance. Because of the dramatic hydrocephalus, this mutant was named big giant head (*bgh*). Homozygous mutants had an enlarged cranial vault indicative of ventricular dilatation (Fig. 1A), which is typically caused by accumulating cerebrospinal fluid in the ventricular system. As a result, the average brain:body ratio for a 3-wk-old *bgh* animal on the B6 background was approximately 2.2 times greater than that of unaffected littermates (Fig. 1B). Histological analysis demonstrated extensive dilatation of the lateral ventricles in *bgh* mutants (Fig. 1, C and D). Intact ependymal cells lining the mutant ventricles possessed histologically normal cilia (Fig. 1E). However, there was evidence of extensive ependymal sloughing and substantial gliosis in the underlying white matter (Fig. 1F). This damage was likely a secondary effect of excessive pressure from accumulating CSF.

The severity of the hydrocephalus in *bgh* homozygotes was variable. For 62 affected B6 animals that died naturally or were euthanized due to severe hydrocephalus at greater than 1 wk of age, the average age of death was 24.5 days. In addition, an undocumented number of animals died within a few days of birth, suggesting that the hydrocephalus may be severe enough to cause perinatal lethality. Of the animals that lived to adulthood, one male lived to 96 days and two males lived to 59 days. One female lived to 28 wk despite the presence of gross hydrocephalus. Because of the unusual lifespan, this outlier was not factored into the average age of death. The mutation was backcrossed to the 129S6/SvEvTac (129) background, and mutant B6129F1 animals were analyzed for the presence of hydrocephalus. Interestingly, animals on the mixed background showed no evidence of gross hydrocephalus, as indicated by a normal cranial vault, and did not exhibit early mortality, despite being infertile and developing sinusitis. This finding indicates the presence of genetic modifiers of the *bgh* hydrocephalus.

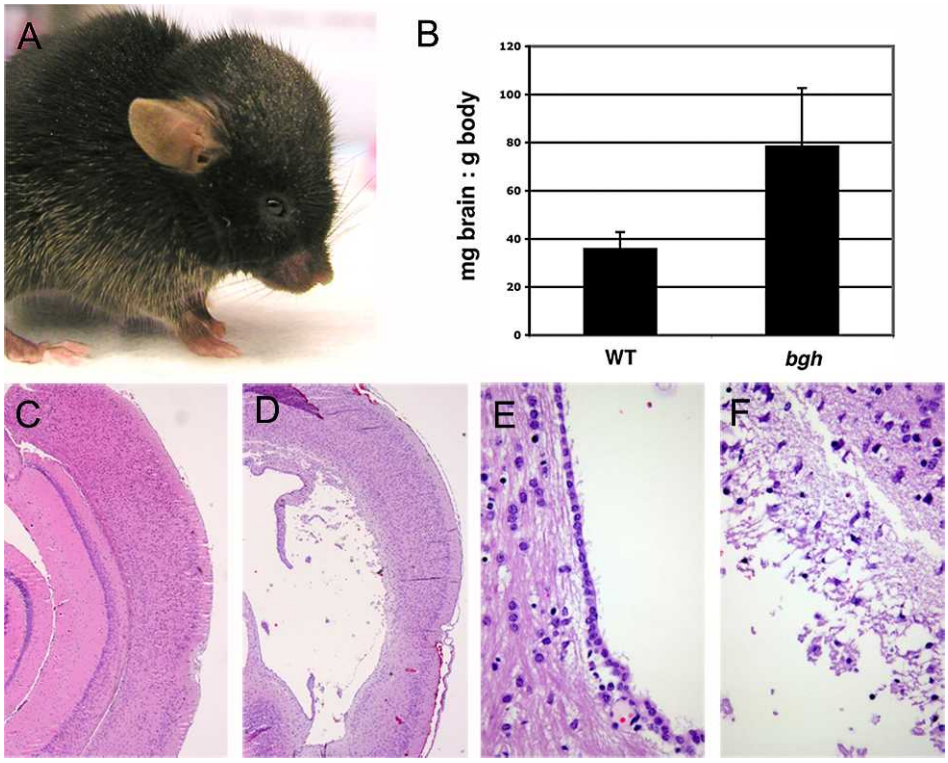

FIG. 1. Hydrocephalus in *bgh* mice. **A**) Gross hydrocephalus in *bgh* homozygote. **B**) Graph showing brain to body ratios for wild type and *bgh* mutants. Ratios are plotted as (mg brain)/(g body). The ratio for *bgh* mutants is approximately 2.2 times greater than that of wild-type animals (n = 8 *bgh* and 4 wild type; $P < 0.005$). **C**–**F**) Coronal sections of wild-type (**C**) and *bgh* (**D**–**F**) brains through the lateral ventricles. Original magnification is 4× (**C**, **D**) or 40× (**E**, **F**). High magnification images show that cilia are present on intact *bgh* ependyma (**E**) and that substantial gliosis has occurred in the *bgh* white matter (**F**). All the sections are stained with hematoxylin and eosin.

bgh *Males Are Infertile Because of Defects in Spermatogenesis*

Although most *bgh* homozygotes on the B6 background died around weaning age, affected animals occasionally lived to adulthood. The inability of wild-type females to become pregnant when paired with mutant males reaching the age of spermatogenesis suggests that the males are infertile. Upon mating, wild-type females paired with three adult B6 *bgh* males for 1–2 wk formed vaginal plugs but did not become pregnant. To further study the infertility phenotype without the complicating factors of severe hydrocephalus and early mortality, homozygous mutant animals were generated on the mixed B6129 background. One *bgh* homozygote on the mixed B6129 background also failed to produce progeny when paired with a wild-type female for 2 wk.

Consistent with the apparent male infertility, histological analysis demonstrated that there were abnormalities during spermiogenesis in the *bgh* testis. The cycle of the seminiferous epithelium is divided into 12 stages (I–XII) in the mouse, with each stage corresponding to a defined arrangement of cell types [96]. There were no obvious defects in the organization of the seminiferous tubules, and spermatogenesis appeared to progress normally in *bgh* mice until the spermatid elongation phase (Fig. 2, A–D). Bundles of elongating spermatids were visible, but there was a reduction in the number of elongating spermatids in stage II–V tubules (Fig. 2, A and B). Those bundles contained nuclei, but no flagellar structures were detectable (Fig. 2, A and B). Stage VII–VIII tubules contained the most mature germ cells just prior to spermiation in the wild-type testis (Fig. 2C). However, very few mature spermatozoa were detected in the *bgh* testis, and the sperm tails appeared to be absent in the lumen of the seminiferous tubule (Fig. 2D). Consistent with this finding in the testis, histological analysis of the *bgh* cauda epididymis revealed the presence of very few mature sperm compared to wild type (Fig. 2, E and F).

The progression of spermatogenesis was further analyzed in staged squash preparations that were isolated on the basis of recognizable transillumination patterns generated by different organizations of condensed elongating spermatid nuclei at specific stages of the seminiferous epithelial cycle [95]. Mouse spermiogenesis is divided into 16 steps, with steps 1–8 comprising the round spermatid phase and steps 9–16 comprising spermatid elongation [95]. Detailed living cell analysis of the squash preparations under phase contrast microscopy confirmed the normal associations of spermatogenic cell types in various stages of *bgh* tubules (Supplemental Fig. S1; all the supplemental data are available online at www.biolreprod.org). Acrosome formation in round spermatids in the early steps of spermiogenesis appeared unaffected (Supplemental Fig. S1). Elongating spermatid bundles were present in stage IV–V tubules, but the orientation of the spermatids inside the bundles was disrupted and a dramatic reduction in the number of bundle-associated elongating spermatids (Supplemental Fig. S1). Stage VII–VIII tubules contained very few mature spermatozoa, and those that were present had abnormally formed flagella (Supplemental Fig. S1). All the *bgh* flagella appeared to be short and disorganized (Supplemental Fig. S1).

Altered Sperm Morphology in bgh *Mice*

To further understand the spermatogenic defect in *bgh* mice, sperm morphology was analyzed by phase contrast microscopy, immunofluorescence, and transmission electron microscopy. Analysis of round and elongating spermatids by phase contrast microscopy showed malformations in sperm flagellar development throughout axonemal formation (Fig. 2, G and H). Abnormally short and disorganized flagella were observed on *bgh* spermatids from steps 8 to 16 (Fig. 2, G and H).

Flagellar malformations were further highlighted by immunofluorescence staining with markers for specific tail structures. Expression of acetylated tubulin, a marker for the

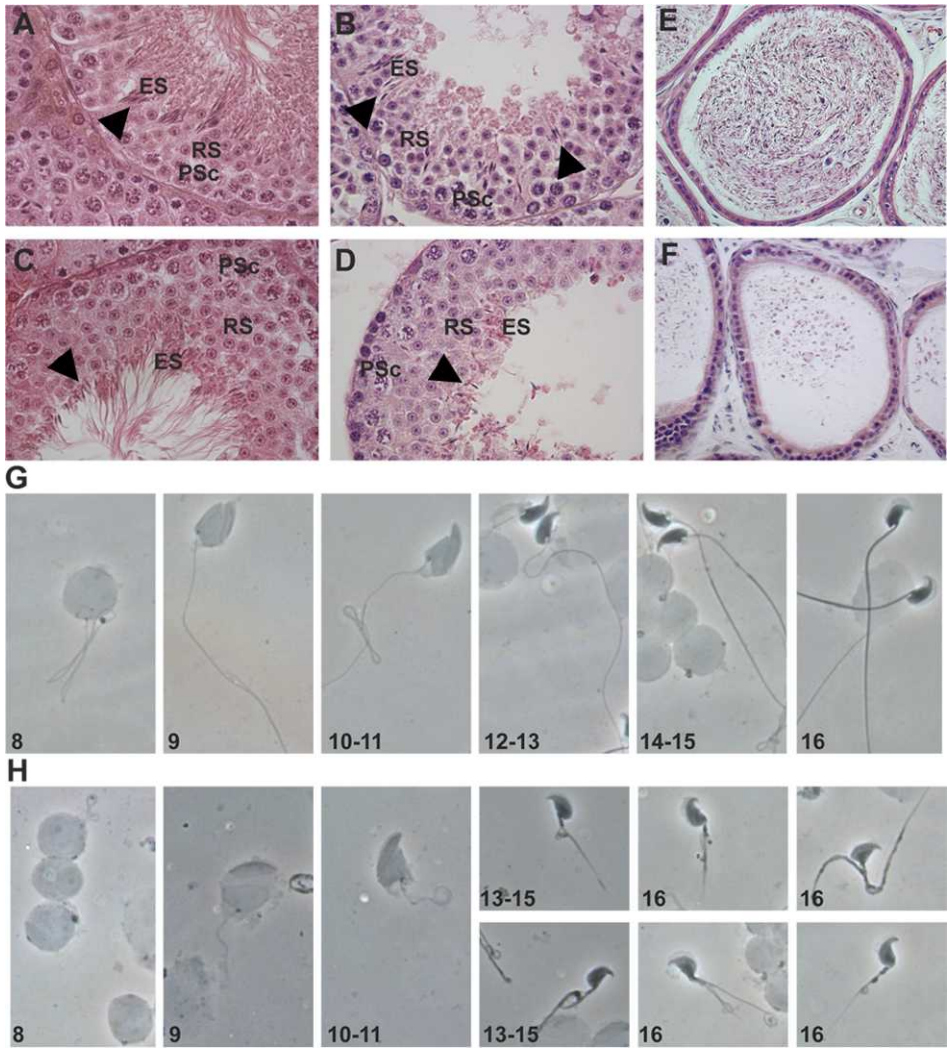

FIG. 2. Males with *bgh* have spermatogenic defects. **A**, **B**) Sections of wild-type (**A**) and *bgh* (**B**) testes showing stage II–V tubules. **C**, **D**) Sections of wild-type (**C**) and *bgh* (**D**) testes showing stage VII–VIII tubules. Original magnification is 40× for all the testis sections. **E**, **F**) Sections of wild-type (**E**) and *bgh* mutant (**F**) cauda epididymis show a reduction in the number of mature sperm. Original magnification is 20×. All histological sections are stained with hematoxylin and eosin. **G**, **H**) Phase contrast microscopy of stage-specific drying down preparations of seminiferous tubules from wild-type (**G**) and *bgh* (**H**) testis. The step of spermatid differentiation (1–16) is indicated in the lower left corner. ES, elongating spermatids; PSc, pachytene spermatocytes; RS, round spermatids.

flagellar axoneme, confirmed that axonemal formation was already disrupted in the spermatids in stage IX–X tubules (Fig. 3, A and B). The shortened tail and disrupted axonemal development were also evident in stage II–V (Fig. 3, C and D) and stage VI–VIII (Fig. 3, E and F) tubules. In addition to axonemal abnormalities, defects in other structures were also apparent. Mitotracker staining showed that mitochondria were either absent from the sperm tail or highly disorganized (Fig. 3, G and H). Absence of fibrous sheath marker AKAP4 in stage II–V (Fig. 3, I and J) and stage VI–VIII (Fig. 3, K and L) tubules also indicated a defect in fibrous sheath formation in *bgh* spermatids. No sperm flagella were correctly assembled in the hundreds of flagella observed in these analyses. Mature sperm isolated from the *bgh* epididymis showed the same flagellar defects observed in *bgh* elongating spermatids. Light microscopic analysis indicated that mutant epididymal sperm had short tails and an abnormal flagellar shape (Fig. 3, M–O). The presence of sperm in the epididymis, albeit in a markedly reduced number, suggested that spermiation was not prevented in *bgh* animals.

Detailed analysis of the *bgh* sperm tail ultrastructure was investigated by transmission electron microscopy. Consistent with data from staged squash preparations, acrosome formation was normal in round and early elongating spermatids (Fig. 4, A–C). In contrast, axonemal abnormalities were already evident at this stage. Recognizable axonemal structures were present, suggesting that flagellar formation was initiated in the *bgh* testis (Fig. 4, D–F). However, there were defects in the microtubule structure that include disorganization or absence of central pair microtubules (Fig. 4, D–F). Disorganization of the microtubules were more extensive in early elongating spermatids (Fig. 4G). By step 16, there was a complete disorganization of the axoneme, mitochondria, and outer dense fibers, and there was a lack of organized fibrous sheath structures (Fig. 4, H–J).

Electron microscopic analysis of epididymal sperm further demonstrated the disorganization of flagellar structures in *bgh* mice. Longitudinal sections showed an absence of recognizable axonemal structures (Fig. 4, K and L). In addition, completed outer dense fiber or fibrous sheath structures were not found (Fig. 4, K and L). Mitochondria, which normally form a sheath along the outer dense fibers in the middle piece, were nearly absent in *bgh* sperm, with only small clusters located near the connecting piece (Fig. 4, K and L). Cross sections of *bgh* sperm flagella further demonstrated the absence of recognizable axonemal structures and the disorganization of mitochondria and outer dense fibers (Fig. 4, M–O). These defects in spermatid elongation and flagellar formation likely account for the infertility in *bgh* mutant males. No mature sperm flagellum was correctly assembled in over 100 flagella observed by electron microscopy. In contrast to the male infertility, *bgh* females are fertile.

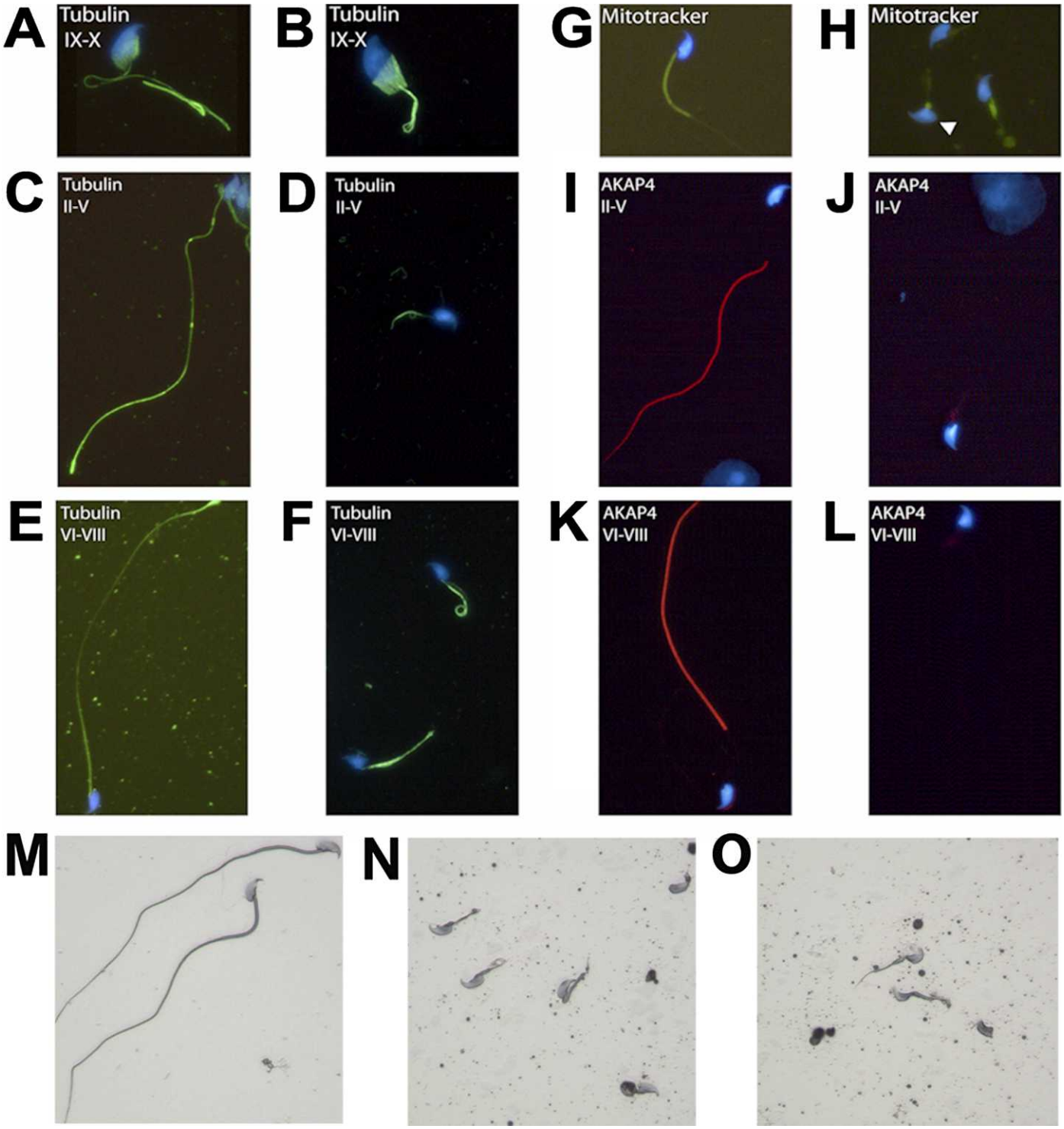

FIG. 3. Abnormal sperm flagellar morphology in *bgh* mutants. **A**–**F**) Immunofluorescence (IF) of axonemal marker acetylated tubulin in wild-type (**A**, **C**, **E**) and *bgh* (**B**, **D**, **F**) seminiferous tubules. **G**, **H**) IF of mitochondrial marker Mitotracker in wild-type (**G**) and *bgh* (**H**) epididymal sperm. **I**–**L**) IF of fibrous sheath marker AKAP4 in wild-type (**I**, **K**) and *bgh* (**J**, **L**) seminiferous tubules. Tubule stages are indicated in the upper left corner of each IF panel. The nucleus is indicated by blue 4′,6-diamidino-2-phenylindole staining in each image. **M**–**O**) Morphology of mature spermatozoa isolated from the cauda epididymis of wild-type (**M**) and *bgh* (**N**, **O**) mice and stained with hematoxylin. Original magnification is 40×.

bgh *Mice Have Sinusitis and a Defect in Ciliary Motility*

In addition to the hydrocephalus and male infertility, *bgh* homozygotes also developed sinusitis. There was an accumulation of mucus in the maxillary sinus cavity of *bgh* animals on the B6 background, and there was a dramatic infiltration of neutrophils, which is indicative of an acute inflammatory response (Fig. 5, A–C). Despite the defects in sperm flagellar formation, electron microscopic analysis of tracheal epithelial cilia indicated that *bgh* cilia were present and ultrastructurally normal (Fig. 5, D–H). Mutant cilia possessed a normal 9+2 axonemal structure, and there were no apparent defects in the dynein arms (Fig. 5, F–H). However, the beat frequency of

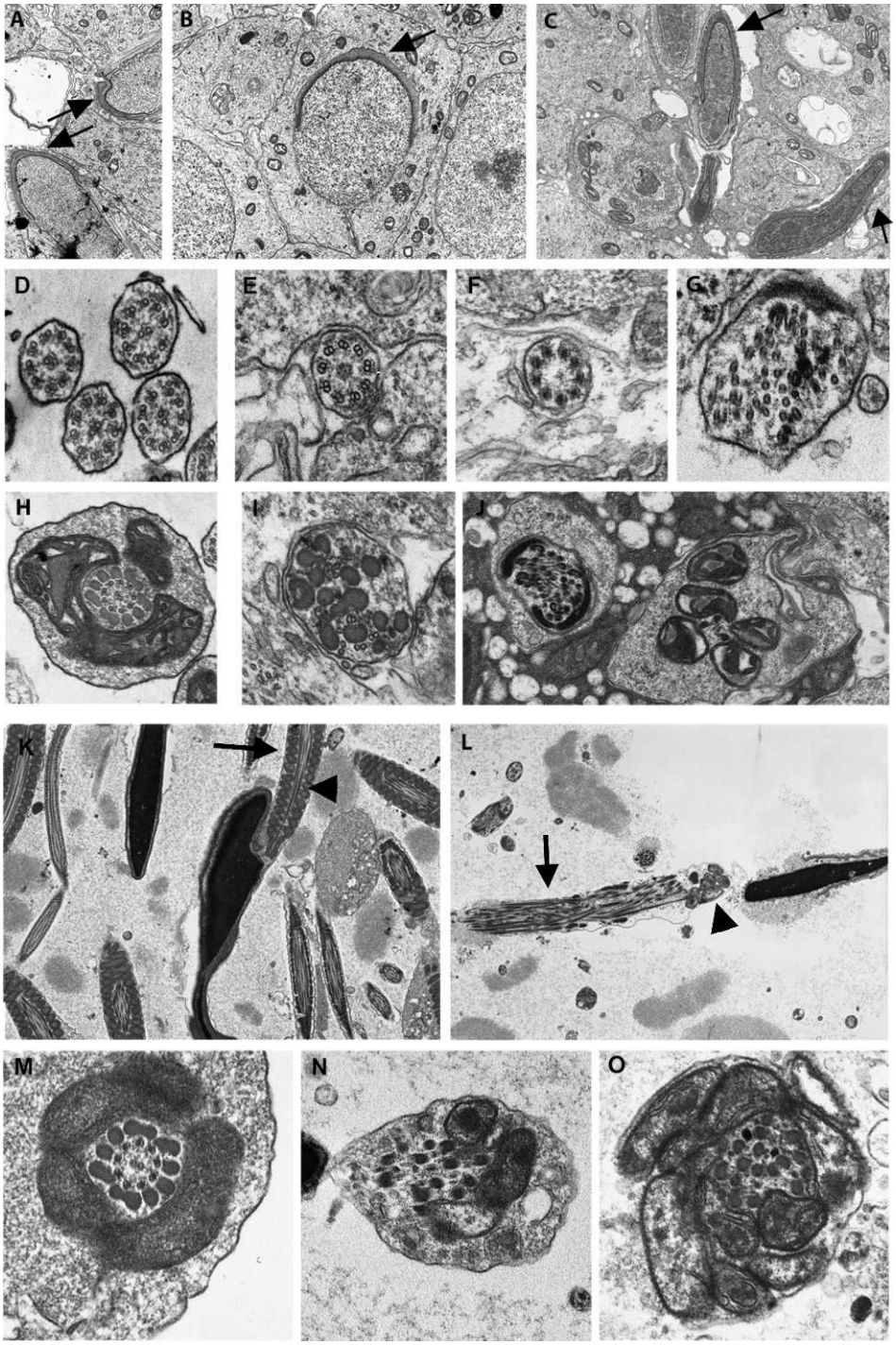

FIG. 4. Transmission electron microscopy showing ultrastructural defects in *bgh* sperm. **A**–**C**) Analysis of the acrosome from wild-type elongating spermatids (**A**), *bgh* round spermatids (**B**), and *bgh* elongating spermatids (**C**). Note the normal appearance of the acrosome (arrows) in *bgh* spermatids. **D**–**J**) Cross sections of the developing spermatid axoneme in wild-type round spermatids (**D**), *bgh* round spermatids (**E**, **F**), *bgh* early elongating spermatids (**G**), wild-type step 15–16 elongating spermatids (**H**), and *bgh* step 15–16 elongating spermatids (**I**, **J**). Microtubule defects including loss of one or both of the central pair tubules are present in *bgh* round spermatids (**E**, **F**), but there is complete disorganization of the axonemal structure by the late elongating spermatid stage (**G**, **I**, **J**). **K**, **L**) Longitudinal sections of epididymal sperm from wild-type (**K**) and *bgh* (**L**) mice. Note the loss of recognizable axonemal or accessory flagellar structures (arrows), the disorganization of mitochondria (arrowheads), and an excess of cytoplasm in the *bgh* sperm (**L**). **M**–**O**) Cross sections of the epididymal sperm flagellum in wild-type (**M**) and *bgh* (**N**, **O**) mice. Note the disorganization of the axoneme and mitochondria in the *bgh* sperm tail (**N**, **O**). Original magnification is 6000× (**A**–**C**, **K**, **L**), 60 000× (**D**–**H**), or 50 000× (**I**, **J**, **M**–**O**).

tracheal epithelial cilia in *bgh* mice was approximately 17% lower than wild-type littermates, with a difference of approximately two beats per second (Fig. 5I). This decrease in ciliary motility presumably accounted for the defect in mucus clearance in the sinus cavity and may also have contributed to a defect in CSF flow in the brain that resulted in hydrocephalus. Mutant animals on the mixed B6129 background also developed sinusitis with a similar accumulation of mucus and infiltration of neutrophils (Supplemental Fig. S2), demonstrating that the PCD was present in mutant animals on this background. Despite the presence of hydrocephalus, male infertility, and sinusitis, situs inversus was not observed in *bgh* mutant mice.

Positional Cloning of the bgh *Gene*

To map the *bgh* mutation, confirmed heterozygotes on the B6 background were crossed to wild-type BALB mice, and F1 heterozygotes were subsequently backcrossed to their heterozygous B6 parent to obtain affected N2 progeny. Using a genomewide screen of affected N2 animals, we mapped the mutation to proximal chromosome 15. Fine mapping with microsatellite markers in the region reduced the *bgh* interval to approximately 8.3 Mb between 3.9 and 12.2 Mb (Fig. 6A). This interval contains 57 genes or novel open reading frames. Candidate genes were prioritized based on known function or expression patterns, and the gene encoding sperm flagellar protein 2 (SPEF2) was considered the top *bgh* candidate gene.

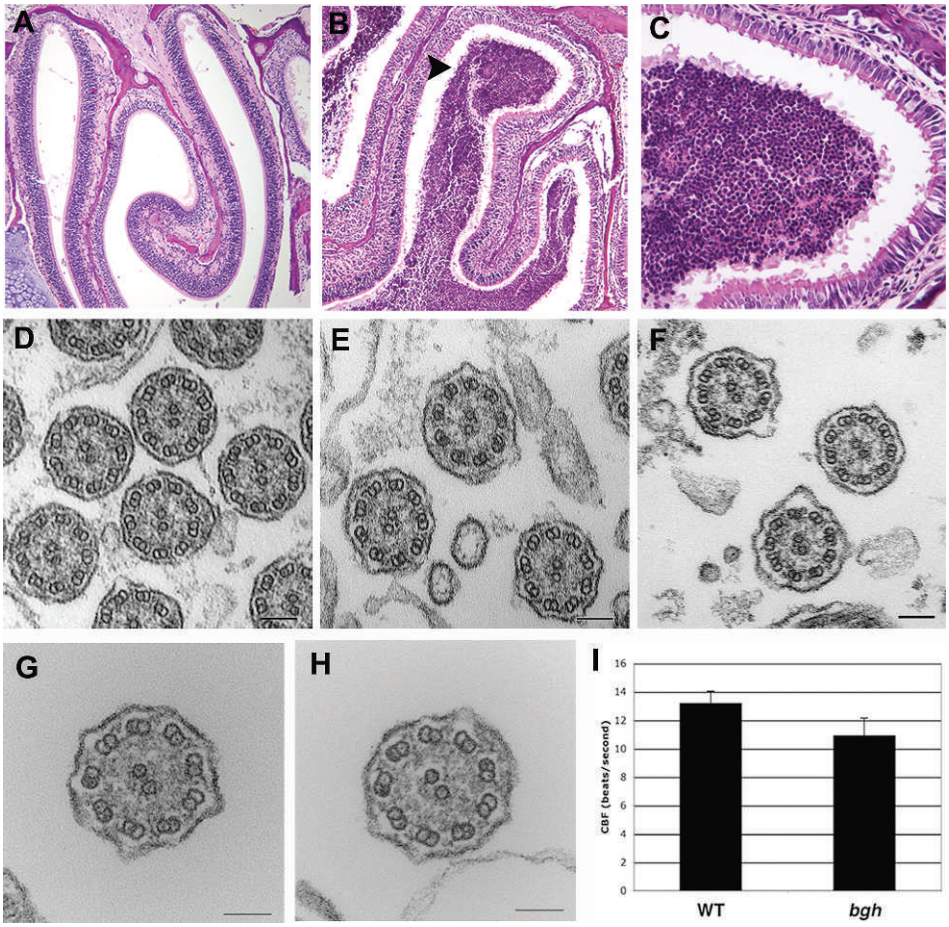

FIG. 5. Sinusitis in *bgh* mice. **A**–**C**) Coronal sections of wild-type (**A**) and *bgh* (**B**, **C**) maxillary sinuses. Note the accumulation of mucus and infiltration of neutrophils in the *bgh* sinuses (arrowhead). Original magnification is 10× (**A**, **B**) or 40× (**C**). Sections are stained with hematoxylin and eosin. **D**–**H**) Electron micrographs showing cross sections of wild-type (**D**, **E**) and *bgh* (**F**–**H**) tracheal epithelial cilia. Note the normal ultrastructure in *bgh* cilia. Relative sizes are indicated by the scale bars. **I**) Analysis of tracheal epithelial ciliary beat frequency (CBF) in beats per second (Hz). The CBF of *bgh* cilia is approximately 17% lower than that of wild-type cilia (n = 9 wild type and 9 *bgh*; $P = 0.03$).

Based on alignment with other species, we determined that the gene and protein sequences in the NCBI and Ensembl databases were incorrectly annotated. To determine the correct gene structure, we used a combination of several methods. We first used online gene prediction programs GeneMark and GenScan to locate potential exons in the genomic sequence spanning this region of chromosome 15. The most likely exons were selected through alignment of the predicted exon sequences with predicted exon sequences from homologs in other mammalian species. Predicated exons were verified by direct sequencing of genomic DNA from wild-type mice. Finally, we verified the location of splice sites as well as the 5′ and 3′ ends of the gene by sequencing reverse transcribed testis cDNA spanning the entire predicted open reading frame. As a result, we determined that the mouse *Spef2* gene was comprised of 37 exons and encoded a predicted protein of 1798 amino acids in the testis. Using the NCBI Conserved Domain search tool, we determined that the SPEF2 predicted protein contained two conserved domains: 1) a domain of unknown function (DUF) from amino acids 5 to 136 and 2) an adenylate kinase domain from amino acids 618 to 800. A calcium-binding EF-hand motif has also been predicted in the porcine homolog [93].

To identify potential disease causing mutations in *Spef2*, we sequenced all 37 exons in *bgh* heterozygous DNA. Sequence analysis revealed two distinct single base substitutions that were confirmed in affected mutants (Fig. 6B). We identified a missense mutation in exon 3 that caused an amino acid substitution of glutamine to lysine in the DUF domain. Substitution of the positively charged lysine for the uncharged glutamine could disrupt folding or function of this domain. In addition, we identified a nonsense mutation in exon 28 that presumably resulted in a truncated protein after amino acid 1320. Although this did not delete any identifiable domains, loss of the C-terminal 26% of the protein could prevent proper protein folding or function. Sequencing of genomic DNA from wild-type B6 and B10 animals indicated that neither of these variants was a common polymorphism, suggesting that either could be a disease-causing mutation. Furthermore, both exons had been sequenced in well over a hundred mice from the *bgh* line, and both mutations were consistent with the presence of the PCD phenotype.

To validate the putative nonsense mutation, a Western blot of wild-type and *bgh* testis lysates was probed with an antibody raised to the C-terminus of SPEF2 [92]. While this antibody detected full-length SPEF2 in wild-type testis, the protein was not detected in the *bgh* testis, suggesting that full-length SPEF2 is absent (Fig. 6C). While it is possible that a missense mutation in exon 3 could cause misfolding and subsequent degradation of SPEF2 that would prevent detection on a Western blot, this finding is more likely due to the nonsense mutation in exon 28, which would result in either a truncated protein or nonsense-mediated decay, thereby providing biochemical validation of this putative mutation. Taken together, these data strongly suggest that the PCD and spermatogenesis defects in *bgh* mice result from the loss of SPEF2 function.

DISCUSSION

In this study, we have shown that loss of SPEF2 function results in PCD with severe spermatogenic defects in the mouse mutant *bgh*. Homozygous mutants have hydrocephalus, male

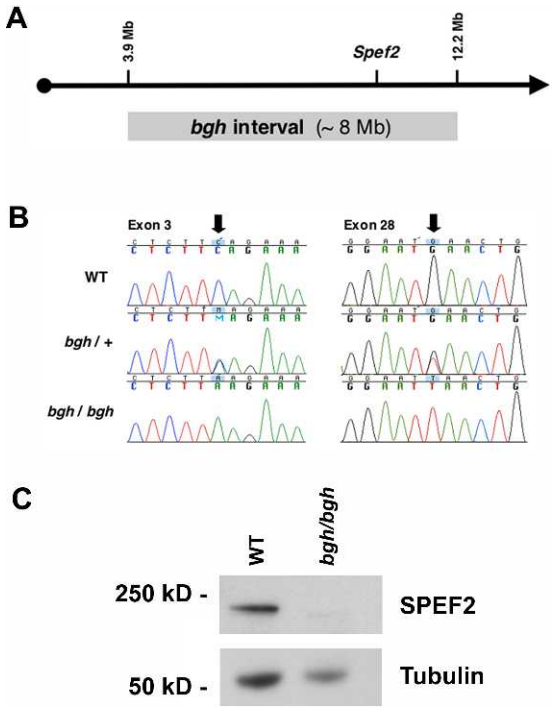

FIG. 6. The *bgh* phenotype results from a mutation in *Spef2*. **A**) Schematic diagram of the *bgh* functional interval, which is defined by a CA repeat microsatellite marker at 3.9 Mb and SNP marker rs13482436 at 12.2 Mb. *Spef2* is the top candidate gene in the interval. The proximal end of chromosome 15 is depicted by an arrow with a circle indicating the acromere. **B**) Sequence chromatograms showing the two putative mutations in *Spef2*. Sequences are shown for wild-type (top), heterozygous (middle), and *bgh* homozygous (bottom) animals for both the missense mutation in exon 3 (left) and the nonsense mutation in exon 28 (right). Each mutated base is indicated by an arrow. **C**) Western blot of SPEF2 in wild-type and *bgh* testis lysates using a polyclonal antibody to the C-terminus of SPEF2. The absence of full-length SPEF2 in the *bgh* testis validates the presence of a nonsense mutation. Acetylated tubulin was used as a control.

infertility, and sinusitis. The infertility results from a reduction in the number of elongating spermatids and mature sperm, as well as structural defects that include short tails and disorganization of axonemal and accessory structures. The sinusitis and hydrocephalus likely result from an observed decrease in ciliary beat frequency.

The morphological and ultrastructural defects associated with *bgh* axonemes and accessory structures likely result from perturbed IFT. Consistent with this hypothesis, SPEF2 has been shown to localize to the sperm manchette and flagellum and interact with the IFT protein IFT20 in the testis [92], which implies a possible role in protein transport during spermatid elongation. Furthermore, mutations in the porcine homolog of *Spef2* result in a similar sperm tail phenotype [93]. In addition to the flagellar defects, slightly abnormal head shapes were also observed in *bgh* sperm, although further studies are required to elucidate the mechanism affecting sperm head development.

Interestingly, despite the defect in spermatogenesis and the absence of 9+2 axonemal structures, *bgh* mutants have a normal respiratory ciliary ultrastructure with a decreased beat frequency. The *bgh* phenotype is very similar to the phenotype that results from loss of the ciliary protein PCDP1 [75]. The *C. reinhardtii* homolog of PCDP1 localizes to the central pair apparatus and regulates ciliary motility in a calcium-dependent pathway [74]. Consistent with this finding, murine SPEF2 is 21% identical to the *C. reinhardtii* protein central pair complex 1 (Cpc1) with conserved DUF and adenylate kinase domains, strongly suggesting that Cpc1 is the *C. reinhardtii* homolog of SPEF2. Cpc1 has been shown to localize to the central pair complex of the *C. reinhardtii* flagellum and interact with central pair protein HYDIN [66, 100]. Therefore, in addition to a role in IFT in the developing spermatid, it is also possible that SPEF2 may localize to the central pair of motile cilia on the respiratory epithelium.

A potential role for SPEF2 in the central pair complex is supported by two pieces of evidence in this study. First, *bgh* cilia are ultrastructurally normal but have a reduced beat frequency, suggesting that SPEF2 may be involved in regulation of ciliary beating rather than ciliogenesis. This is in contrast to the ultrastructural defects observed in sperm flagella, which appear in round spermatids and become more severe as spermiogenesis progresses. Second, the absence of situs inversus in *bgh* mice suggests that SPEF2 does not play a critical role in nodal cilia, which do not possess a central microtubule pair. A role for SPEF2 in the central pair is consistent with human mutations that affect the central pair and result in PCD without situs inversus [101] as well as the absence of situs inversus in mice lacking *Pcdp1* [75]. It is therefore possible that SPEF2 has multiple, tissue-specific functions. In epithelial and ependymal cilia, it may localize to the central pair and regulate ciliary motility, whereas in the testis, it is essential for spermatid elongation and likely functions in IFT. This is supported by the finding that full-length SPEF2 is testis-specific [92], despite the presence of hydrocephalus and sinusitis in *bgh* mice. This is also consistent with colocalization of SPEF2 with IFT20 in the Golgi of developing spermatids and flagellar localization of SPEF2 in mature sperm [92], suggesting that SPEF2 may have distinct roles in elongating spermatids and mature flagella. Further studies are required to fully understand the biochemical function of SPEF2 in these various cell types; however, these studies suggest that, despite the structural similarities between cilia and flagella, there appear to be fundamental differences in the biogenesis and regulation of the two organelles.

Although the presence of the nonsense mutation in exon 28 was validated by Western blot analysis, it is possible that both mutations in *Spef2* result in the same *bgh* phenotype. Alternatively, because full-length SPEF2 was shown to be testis-specific [92] and a mutation in the exon homologous to 28 in Finnish Yorkshire pigs causes only sperm tail defects [92], the ciliary abnormalities could be caused by the missense mutation in exon 3, while loss of the C-terminus could specifically result in the spermatogenic defects. It is also possible that the missense mutation in exon 3 is a passenger mutation from the original ENU mutagenesis [94] and that the PCD phenotypes result solely from the nonsense mutation in exon 28. Based on sequencing of genomic DNA from B6 and B10 animals, it is unlikely that either variant is a common polymorphism.

To date, no mutations have been identified in the human ortholog of *Spef2* that result in PCD. However, given the severity of the phenotype, studies elucidating the function of SPEF2 will continue to reveal the molecular mechanisms that regulate ciliary function and spermatogenesis. These studies will likely contribute to improved understanding, diagnosis, and treatment of male infertility and PCD.

ACKNOWLEDGMENTS

We gratefully thank Robin Haynes for assisting with the analysis of the neuropathology and Sherika Blevins for assistance with the mouse husbandry.

REFERENCES

1. Ahmed EA, de Rooij DG. Staging of mouse seminiferous tubule cross-sections. Methods Mol Biol 2009; 558:263–277.
2. Clermont Y. Kinetics of spermatogenesis in mammals: seminiferous epithelium cycle and spermatogonial renewal. Physiol Rev 1972; 52:198–236.
3. Hermo L, Pelletier RM, Cyr DG, Smith CE. Surfing the wave, cycle, life history, and genes/proteins expressed by testicular germ cells. Part 1: background to spermatogenesis, spermatogonia, and spermatocytes. Microsc Res Tech 2010; 73:241–278.
4. Hermo L, Pelletier RM, Cyr DG, Smith CE. Surfing the wave, cycle, life history, and genes/proteins expressed by testicular germ cells. Part 2: changes in spermatid organelles associated with development of spermatozoa. Microsc Res Tech 2010; 73:279–319.
5. Hermo L, Pelletier RM, Cyr DG, Smith CE. Surfing the wave, cycle, life history, and genes/proteins expressed by testicular germ cells. Part 5: intercellular junctions and contacts between germs cells and Sertoli cells and their regulatory interactions, testicular cholesterol, and genes/proteins associated with more than one germ cell generation. Microsc Res Tech 2010; 73:409–494.
6. Hermo L, Pelletier RM, Cyr DG, Smith CE. Surfing the wave, cycle, life history, and genes/proteins expressed by testicular germ cells. Part 4: intercellular bridges, mitochondria, nuclear envelope, apoptosis, ubiquitination, membrane/voltage-gated channels, methylation/acetylation, and transcription factors. Microsc Res Tech 2010; 73:364–408.
7. Hermo L, Pelletier RM, Cyr DG, Smith CE. Surfing the wave, cycle, life history, and genes/proteins expressed by testicular germ cells. Part 3: developmental changes in spermatid flagellum and cytoplasmic droplet and interaction of sperm with the zona pellucida and egg plasma membrane. Microsc Res Tech 2010; 73:320–363.
8. Hess RA. Quantitative and qualitative characteristics of the stages and transitions in the cycle of the rat seminiferous epithelium: light microscopic observations of perfusion-fixed and plastic-embedded testes. Biol Reprod 1990; 43:525–542.
9. Leblond CP, Clermont Y. Definition of the stages of the cycle of the seminiferous epithelium in the rat. Ann N Y Acad Sci 1952; 55:548–573.
10. Oakberg EF. Duration of spermatogenesis in the mouse and timing of stages of the cycle of the seminiferous epithelium. Am J Anat 1956; 99:507–516.
11. Oakberg EF. A description of spermiogenesis in the mouse and its use in analysis of the cycle of the seminiferous epithelium and germ cell renewal. Am J Anat 1956; 99:391–413.
12. Parvinen M. Regulation of the seminiferous epithelium. Endocr Rev 1982; 3:404–417.
13. Yan W. Male infertility caused by spermiogenic defects: lessons from gene knockouts. Mol Cell Endocrinol 2009; 306:24–32.
14. Mruk DD, Cheng CY. Sertoli-Sertoli and Sertoli-germ cell interactions and their significance in germ cell movement in the seminiferous epithelium during spermatogenesis. Endocr Rev 2004; 25:747–806.
15. Petersen C, Soder O. The sertoli cell—a hormonal target and 'super' nurse for germ cells that determines testicular size. Horm Res 2006; 66:153–161.
16. Irons MJ. Synthesis and assembly of connecting-piece proteins as revealed by radioautography. J Ultrastruct Res 1983; 82:27–34.
17. Lee L. Mechanisms of mammalian ciliary motility: insights from primary ciliary dyskinesia genetics. Gene 2011; 473:57–66.
18. Oko RJ, Clermont Y. Biogenesis of specialized cytoskeletal elements of rat spermatozoa. Ann N Y Acad Sci 1991; 637:203–223.
19. Clermont Y, Oko R, Hermo L. Immunocytochemical localization of proteins utilized in the formation of outer dense fibers and fibrous sheath in rat spermatids: an electron microscope study. Anat Rec 1990; 227:447–457.
20. Irons MJ, Clermont Y. Formation of the outer dense fibers during spermiogenesis in the rat. Anat Rec 1982; 202:463–471.
21. Oko R, Clermont Y. Light microscopic immunocytochemical study of fibrous sheath and outer dense fiber formation in the rat spermatid. Anat Rec 1989; 225:46–55.
22. Eddy EM, Toshimori K, O'Brien DA. Fibrous sheath of mammalian spermatozoa. Microsc Res Tech 2003; 61:103–115.
23. Irons MJ, Clermont Y. Kinetics of fibrous sheath formation in the rat spermatid. Am J Anat 1982; 165:121–130.
24. Bisgrove BW, Yost HJ. The roles of cilia in developmental disorders and disease. Development 2006; 133:4131–4143.
25. Hirokawa N, Tanaka Y, Okada Y, Takeda S. Nodal flow and the generation of left-right asymmetry. Cell 2006; 125:33–45.
26. Satir P, Christensen ST. Overview of structure and function of mammalian cilia. Annu Rev Physiol 2007; 69:377–400.
27. Stannard W, O'Callaghan C. Ciliary function and the role of cilia in clearance. J Aerosol Med 2006; 19:110–115.
28. Zariwala MA, Knowles MR, Omran H. Genetic defects in ciliary structure and function. Annu Rev Physiol 2007; 69:423–450.
29. Scholey JM. Intraflagellar transport motors in cilia: moving along the cell's antenna. J Cell Biol 2008; 180:23–29.
30. Afzelius BA. A human syndrome caused by immotile cilia. Science 1976; 193:317–319.
31. Leigh MW, Pittman JE, Carson JL, Ferkol TW, Dell SD, Davis SD, Knowles MR, Zariwala MA. Clinical and genetic aspects of primary ciliary dyskinesia/Kartagener syndrome. Genet Med 2009; 11:473–487.
32. Van's Gravesande KS, Omran H. Primary ciliary dyskinesia: clinical presentation, diagnosis and genetics. Ann Med 2005; 37:439–449.
33. al-Shroof M, Karnik AM, Karnik AA, Longshore J, Sliman NA, Khan FA. Ciliary dyskinesia associated with hydrocephalus and mental retardation in a Jordanian family. Mayo Clin Proc 2001; 76:1219–1224.
34. De Santi MM, Magni A, Valletta EA, Gardi C, Lungarella G. Hydrocephalus, bronchiectasis, and ciliary aplasia. Arch Dis Child 1990; 65:543–544.
35. Greenstone MA, Jones RW, Dewar A, Neville BG, Cole PJ. Hydrocephalus and primary ciliary dyskinesia. Arch Dis Child 1984; 59:481–482.
36. Jabourian Z, Lublin FD, Adler A, Gonzales C, Northrup B, Zwillenberg D. Hydrocephalus in Kartagener's syndrome. Ear Nose Throat J 1986; 65:468–472.
37. Kosaki K, Ikeda K, Miyakoshi K, Ueno M, Kosaki R, Takahashi D, Tanaka M, Torikata C, Yoshimura Y, Takahashi T. Absent inner dynein arms in a fetus with familial hydrocephalus-situs abnormality. Am J Med Genet A 2004; 129A:308–311.
38. Zammarchi E, Calzolari C, Pignotti MS, Pezzati P, Lignana E, Cama A. Unusual presentation of the immotile cilia syndrome in two children. Acta Paediatr 1993; 82:312–313.
39. Duquesnoy P, Escudier E, Vincensini L, Freshour J, Bridoux AM, Coste A, Deschildre A, de Blic J, Legendre M, Montantin G, Tenreiro H, Vojtek AM, et al. Loss-of-function mutations in the human ortholog of Chlamydomonas reinhardtii ODA7 disrupt dynein arm assembly and cause primary ciliary dyskinesia. Am J Hum Genet 2009; 85:890–896.
40. Duriez B, Duquesnoy P, Escudier E, Bridoux AM, Escalier D, Rayet I, Marcos E, Vojtek AM, Bercher JF, Amselem S. A common variant in combination with a nonsense mutation in a member of the thioredoxin family causes primary ciliary dyskinesia. Proc Natl Acad Sci U S A 2007; 104:3336–3341.
41. Guichard C, Harricane MC, Lafitte JJ, Godard P, Zaegel M, Tack V, Lalau G, Bouvagnet P. Axonemal dynein intermediate-chain gene (DNAI1) mutations result in situs inversus and primary ciliary dyskinesia (Kartagener syndrome). Am J Hum Genet 2001; 68:1030–1035.
42. Loges NT, Olbrich H, Fenske L, Mussaffi H, Horvath J, Fliegauf M, Kuhl H, Baktai G, Peterffy E, Chodhari R, Chung EM, Rutman A, et al. DNAI2 mutations cause primary ciliary dyskinesia with defects in the outer dynein arm. Am J Hum Genet 2008; 83:547–558.
43. Mygind N, Pedersen M. Nose-, sinus- and ear-symptoms in 27 patients with primary ciliary dyskinesia. Eur J Respir Dis Suppl 1983; 127:96–101.
44. Nastasi KJ, Blaiss MS. A seven-year-old boy with sinusitis, otitis media, and asthma. Ann Allergy 1994; 73:15–20.
45. Omran H, Kobayashi D, Olbrich H, Tsukahara T, Loges NT, Hagiwara H, Zhang Q, Leblond G, O'Toole E, Hara C, Mizuno H, Kawano H, et al. Ktu/PF13 is required for cytoplasmic pre-assembly of axonemal dyneins. Nature 2008; 456:611–616.
46. Pedersen M, Mygind N. Rhinitis, sinusitis and otitis media in Kartagener's syndrome (primary ciliary dyskinesia). Clin Otolaryngol Allied Sci 1982; 7:373–380.
47. Halbert SA, Patton DL, Zarutskie PW, Soules MR. Function and structure of cilia in the fallopian tube of an infertile woman with Kartagener's syndrome. Hum Reprod 1997; 12:55–58.
48. Lurie M, Tur-Kaspa I, Weill S, Katz I, Rabinovici J, Goldenberg S. Ciliary ultrastructure of respiratory and fallopian tube epithelium in a sterile woman with Kartagener's syndrome. A quantitative estimation. Chest 1989; 95:578–581.
49. McComb P, Langley L, Villalon M, Verdugo P. The oviductal cilia and Kartagener's syndrome. Fertil Steril 1986; 46:412–416.
50. Pedersen H. Absence of dynein arms in endometrial cilia: cause of infertility? Acta Obstet Gynecol Scand 1983; 62:625–627.
51. Moore A, Escudier E, Roger G, Tamalet A, Pelosse B, Marlin S, Clement

A, Geremek M, Delaisi B, Bridoux AM, Coste A, Witt M, et al. RPGR is mutated in patients with a complex X linked phenotype combining primary ciliary dyskinesia and retinitis pigmentosa. J Med Genet 2006; 43:326–333.
52. van Dorp DB, Wright AF, Carothers AD, Bleeker-Wagemakers EM. A family with RP3 type of X-linked retinitis pigmentosa: an association with ciliary abnormalities. Hum Genet 1992; 88:331–334.
53. Zito I, Downes SM, Patel RJ, Cheetham ME, Ebenezer ND, Jenkins SA, Bhattacharya SS, Webster AR, Holder GE, Bird AC, Bamiou DE, Hardcastle AJ. RPGR mutation associated with retinitis pigmentosa, impaired hearing, and sinorespiratory infections. J Med Genet 2003; 40:609–615.
54. Escudier E, Duquesnoy P, Papon JF, Anselem S. Ciliary defects and genetics of primary ciliary dyskinesia. Paediatr Respir Rev 2009; 10:51–54.
55. Hornef N, Olbrich H, Horvath J, Zariwala MA, Fliegauf M, Loges NT, Wildhaber J, Noone PG, Kennedy M, Antonarakis SE, Blouin JL, Bartoloni L, et al. DNAH5 mutations are a common cause of primary ciliary dyskinesia with outer dynein arm defects. Am J Respir Crit Care Med 2006; 174:120–126.
56. Ibanez-Tallon I, Gorokhova S, Heintz N. Loss of function of axonemal dynein Mdnah5 causes primary ciliary dyskinesia and hydrocephalus. Hum Mol Genet 2002; 11:715–721.
57. Ibanez-Tallon I, Pagenstecher A, Fliegauf M, Olbrich H, Kispert A, Ketelsen UP, North A, Heintz N, Omran H. Dysfunction of axonemal dynein heavy chain Mdnah5 inhibits ependymal flow and reveals a novel mechanism for hydrocephalus formation. Hum Mol Genet 2004; 13:2133–2141.
58. Olbrich H, Haffner K, Kispert A, Volkel A, Volz A, Sasmaz G, Reinhardt R, Hennig S, Lehrach H, Konietzko N, Zariwala M, Noone PG, et al. Mutations in DNAH5 cause primary ciliary dyskinesia and randomization of left-right asymmetry. Nat Genet 2002; 30:143–144.
59. Neesen J, Kirschner R, Ochs M, Schmiedl A, Habermann B, Mueller C, Holstein AF, Nuesslein T, Adham I, Engel W. Disruption of an inner arm dynein heavy chain gene results in asthenozoospermia and reduced ciliary beat frequency. Hum Mol Genet 2001; 10:1117–1128.
60. Bartoloni L, Blouin JL, Pan Y, Gehrig C, Maiti AK, Scamuffa N, Rossier C, Jorissen M, Armengot M, Meeks M, Mitchison HM, Chung EM, et al. Mutations in the DNAH11 (axonemal heavy chain dynein type 11) gene cause one form of situs inversus totalis and most likely primary ciliary dyskinesia. Proc Natl Acad Sci U S A 2002; 99:10282–10286.
61. Pifferi M, Michelucci A, Conidi ME, Cangiotti AM, Simi P, Macchia P, Boner AL. New DNAH11 mutations in primary ciliary dyskinesia with normal axonemal ultrastructure. Eur Respir J 2010; 35:1413–1416.
62. Schwabe GC, Hoffmann K, Loges NT, Birker D, Rossier C, de Santi MM, Olbrich H, Fliegauf M, Failly M, Liebers U, Collura M, Gaedicke G, et al. Primary ciliary dyskinesia associated with normal axoneme ultrastructure is caused by DNAH11 mutations. Hum Mutat 2008; 29:289–298.
63. Ostrowski LE, Yin W, Rogers TD, Busalacchi KB, Chua M, O'Neal WK, Grubb BR. Conditional deletion of dnaic1 in a murine model of primary ciliary dyskinesia causes chronic rhinosinusitis. Am J Respir Cell Mol Biol 2010; 43:55–63.
64. Berry RJ. The inheritance and pathogenesis of hydrocephalus-3 in the mouse. J Path Bact 1961; 81:157–167.
65. Davy BE, Robinson ML. Congenital hydrocephalus in hy3 mice is caused by a frameshift mutation in Hydin, a large novel gene. Hum Mol Genet 2003; 12:1163–1170.
66. Lechtreck KF, Witman GB. Chlamydomonas reinhardtii hydin is a central pair protein required for flagellar motility. J Cell Biol 2007; 176:473–482.
67. Lechtreck KF, Delmotte P, Robinson ML, Sanderson MJ, Witman GB. Mutations in Hydin impair ciliary motility in mice. J Cell Biol 2008; 180:633–643.
68. Raimondi AJ, Bailey OT, McLone DG, Lawson RF, Echeverry A. The pathophysiology and morphology of murine hydrocephalus in Hy-3 and Ch mutants. Surg Neurol 1973; 1:50–55.
69. Sapiro R, Kostetskii I, Olds-Clarke P, Gerton GL, Radice GL, Strauss IJ. Male infertility, impaired sperm motility, and hydrocephalus in mice deficient in sperm-associated antigen 6. Mol Cell Biol 2002; 22:6298–6305.
70. Smith EF, Lefebvre PA. PF16 encodes a protein with armadillo repeats and localizes to a single microtubule of the central apparatus in Chlamydomonas flagella. J Cell Biol 1996; 132:359–370.
71. Zhang Z, Tang W, Zhou R, Shen X, Wei Z, Patel AM, Povlishock JT, Bennett J, Strauss JF III. Accelerated mortality from hydrocephalus and pneumonia in mice with a combined deficiency of SPAG6 and SPAG16L reveals a functional interrelationship between the two central apparatus proteins. Cell Motil Cytoskeleton 2007; 64:360–376.
72. Smith EF, Lefebvre PA. PF20 gene product contains WD repeats and localizes to the intermicrotubule bridges in Chlamydomonas flagella. Mol Biol Cell 1997; 8:455–467.
73. Zhang Z, Kostetskii I, Tang W, Haig-Ladewig L, Sapiro R, Wei Z, Patel AM, Bennett J, Gerton GL, Moss SB, Radice GL, Strauss JF III. Deficiency of SPAG16L causes male infertility associated with impaired sperm motility. Biol Reprod 2006; 74:751–759.
74. DiPetrillo CG, Smith EF. Pcdp1 is a central apparatus protein that binds Ca(2+)-calmodulin and regulates ciliary motility. J Cell Biol 2010; 189:601–612.
75. Lee L, Campagna DR, Pinkus JL, Mulhern H, Wyatt TA, Sisson JH, Pavlik JA, Pinkus GS, Fleming MD. Primary ciliary dyskinesia in mice lacking the novel ciliary protein Pcdp1. Mol Cell Biol 2008; 28:949–957.
76. Castleman VH, Romio L, Chodhari R, Hirst RA, de Castro SC, Parker KA, Ybot-Gonzalez P, Emes RD, Wilson SW, Wallis C, Johnson CA, Herrera RJ, et al. Mutations in radial spoke head protein genes RSPH9 and RSPH4A cause primary ciliary dyskinesia with central-microtubular-pair abnormalities. Am J Hum Genet 2009; 84:197–209.
77. Murcia NS, Richards WG, Yoder BK, Mucenski ML, Dunlap JR, Woychik RP. The Oak Ridge Polycystic Kidney (orpk) disease gene is required for left-right axis determination. Development 2000; 127:2347–2355.
78. Taulman PD, Haycraft CJ, Balkovetz DF, Yoder BK. Polaris, a protein involved in left-right axis patterning, localizes to basal bodies and cilia. Mol Biol Cell 2001; 12:589–599.
79. Tanaka H, Iguchi N, Toyama Y, Kitamura K, Takahashi T, Kaseda K, Maekawa M, Nishimune Y. Mice deficient in the axonemal protein Tektin-t exhibit male infertility and immotile-cilium syndrome due to impaired inner arm dynein function. Mol Cell Biol 2004; 24:7958–7964.
80. Loges NT, Olbrich H, Becker-Heck A, Haffner K, Heer A, Reinhard C, Schmidts M, Kispert A, Zariwala MA, Leigh MW, Knowles MR, Zentgraf H, et al. Deletions and point mutations of LRRC50 cause primary ciliary dyskinesia due to dynein arm defects. Am J Hum Genet 2009; 85:883–889.
81. Brody SL, Yan XH, Wuerffel MK, Song SK, Shapiro SD. Ciliogenesis and left-right axis defects in forkhead factor HFH-4-null mice. Am J Respir Cell Mol Biol 2000; 23:45–51.
82. Chen J, Knowles HJ, Hebert JL, Hackett BP. Mutation of the mouse hepatocyte nuclear factor/forkhead homologue 4 gene results in an absence of cilia and random left-right asymmetry. J Clin Invest 1998; 102:1077–1082.
83. Takaki E, Fujimoto M, Nakahari T, Yonemura S, Miyata Y, Hayashida N, Yamamoto K, Vallee RB, Mikuriya T, Sugahara K, Yamashita H, Inouye S, et al. Heat shock transcription factor 1 is required for maintenance of ciliary beating in mice. J Biol Chem 2007; 282:37285–37292.
84. Kobayashi Y, Watanabe M, Okada Y, Sawa H, Takai H, Nakanishi M, Kawase Y, Suzuki H, Nagashima K, Ikeda K, Motoyama N. Hydrocephalus, situs inversus, chronic sinusitis, and male infertility in DNA polymerase lambda-deficient mice: possible implication for the pathogenesis of immotile cilia syndrome. Mol Cell Biol 2002; 22:2769–2776.
85. Voronina VA, Takemaru K, Treuting P, Love D, Grubb BR, Hajjar AM, Adams A, Li FQ, Moon RT. Inactivation of Chibby affects function of motile airway cilia. J Cell Biol 2009; 185:225–233.
86. Fernandez-Gonzalez A, Kourembanas S, Wyatt TA, Mitsialis SA. Mutation of murine adenylate kinase 7 underlies a primary ciliary dyskinesia phenotype. Am J Respir Cell Mol Biol 2009; 40:305–313.
87. Ikegami K, Sato S, Nakamura K, Ostrowski LE, Setou M. Tubulin polyglutamylation is essential for airway ciliary function through the regulation of beating asymmetry. Proc Natl Acad Sci U S A 2010; 107:10490–10495.
88. Vogel P, Hansen G, Fontenot G, Read R. Tubulin tyrosine ligase-like 1 deficiency results in chronic rhinosinusitis and abnormal development of spermatid flagella in mice. Vet Pathol 2010; 47:703–712.
89. Ostrowski LE, Blackburn K, Radde KM, Moyer MB, Schlatzer DM, Moseley A, Boucher RC. A proteomic analysis of human cilia: identification of novel components. Mol Cell Proteomics 2002; 1:451–465.
90. Pazour GJ, Agrin N, Leszyk J, Witman GB. Proteomic analysis of a eukaryotic cilium. J Cell Biol 2005; 170:103–113.
91. Ostrowski LE, Andrews K, Potdar P, Matsuura H, Jetten A, Nettesheim P. Cloning and characterization of KPL2, a novel gene induced during

ciliogenesis of tracheal epithelial cells. Am J Respir Cell Mol Biol 1999; 20:675–683.
92. Sironen A, Hansen J, Thomsen B, Andersson M, Vilkki J, Toppari J, Kotaja N. Expression of SPEF2 during mouse spermatogenesis and identification of IFT20 as an interacting protein. Biol Reprod 2010; 82:580–590.
93. Sironen A, Thomsen B, Andersson M, Ahola V, Vilkki J. An intronic insertion in KPL2 results in aberrant splicing and causes the immotile short-tail sperm defect in the pig. Proc Natl Acad Sci U S A 2006; 103:5006–5011.
94. Lambe T, Simpson RJ, Dawson S, Bouriez-Jones T, Crockford TL, Lepherd M, Latunde-Dada GO, Robinson H, Raja KB, Campagna DR, Villarreal G Jr, Ellory JC, et al. Identification of a Steap3 endosomal targeting motif essential for normal iron metabolism. Blood 2009; 113:1805–1808.
95. Kotaja N, Kimmins S, Brancorsini S, Hentsch D, Vonesch JL, Davidson I, Parvinen M, Sassone-Corsi P. Preparation, isolation and characterization of stage-specific spermatogenic cells for cellular and molecular analysis. Nat Methods 2004; 1:249–254.
96. Sisson JH, Stoner JA, Ammons BA, Wyatt TA. All-digital image capture and whole-field analysis of ciliary beat frequency. J Microsc 2003; 211:103–111.
97. Lomsadze A, Ter-Hovhannisyan V, Chernoff YO, Borodovsky M. Gene identification in novel eukaryotic genomes by self-training algorithm. Nucleic Acids Res 2005; 33:6494–6506.
98. Burge C, Karlin S. Prediction of complete gene structures in human genomic DNA. J Mol Biol 1997; 268:78–94.
99. Marchler-Bauer A, Bryant SH. CD-Search: protein domain annotations on the fly. Nucleic Acids Res 2004; 32:W327–W331.
100. Zhang H, Mitchell DR. Cpc1, a Chlamydomonas central pair protein with an adenylate kinase domain. J Cell Sci 2004; 117:4179–4188.
101. Stannard W, Rutman A, Wallis C, O'Callaghan C. Central microtubular agenesis causing primary ciliary dyskinesia. Am J Respir Crit Care Med 2004; 169:634–637.